

Antireflection of Optical Anisotropic Dielectric Metasurfaces

Yu-Hsuan Liao

National Central University

Wei-Lun Hsu

National Central University

Chin-Ming Wang (✉ cmwang@cc.ncu.edu.tw)

National Central University

Article

Keywords:

Posted Date: March 14th, 2022

DOI: <https://doi.org/10.21203/rs.3.rs-1437876/v1>

License: © ⓘ This work is licensed under a Creative Commons Attribution 4.0 International License.

[Read Full License](#)

Abstract

We propose a hetero-nano-fin structure to further improve the efficiency of Pancharatnam–Berry phase metasurfaces. Two hetero-nano-fin types, MgF_2/GaN and $\text{MgF}_2/\text{Nb}_2\text{O}_5$, were investigated. The overall polarization conversion efficiency (PCE) improved from 52.7% to 54% for the MgF_2/GaN nano-fin compared with the bare GaN nano-fin. The overall PCE of the Nb_2O_5 nano-fin was 1.7 times higher than that of the GaN nano-fin. The overall PCE improved from 92.4% up to 96% after the application of MgF_2 antireflection. Although the increment of energy seems minimal, antireflection is crucial for a metasurface, not only enhancing efficiency but also reducing background signal of a meta-device.

Introduction

Plasmonic metasurfaces, consisting of two-dimensional metallic meta-atom arrays, are advantageous because of their properties such as ultrathin thicknesses, ease of fabrication, versatile functionality, field confinement beyond the diffraction limit, and superior nonlinearity^{1–6}. Although a plasmonic metasurface has an impressive light modulation ability, its efficiency is limited as it suffers from Ohmic heat loss during resonance. Huygens meta-atoms, which are meta-atoms in which resonances of the electric dipole and magnetic dipole coincide, can break the scattering symmetry and improve the transmission efficiency^{7,8}. Although zero back-scattering can be achieved under the first Kerker condition⁹, the transmission efficiency of a plasmonic metasurface is limited at a visible frequency.

A dielectric metasurface almost effortlessly avoids Ohmic heat loss and has therefore rapidly attracted extensive research attention. In addition to resonance-based light modulation, the dielectric metasurface is generally capable of two typical light modulation methods: propagation phase^{10–14} and geometric phase^{15–21}. The propagation phase involves phase accumulation during light propagation. For a fixed propagation path, the effective index of the metasurface determines the optical path difference (OPD), such as controlling the filling ratio of the material. The geometric phase is also termed the Pancharatnam–Berry (PB) phase. Light carries an additional phase when it passes through an optical anisotropic structure/material. Spatially varying geometric orientation of the optical anisotropic structure can control phase distribution. Moreover, the original polarization state of light changes to the orthogonal one (e.g., left-hand circular polarization to right-hand circular polarization) and carries geometric phase modulation. Therefore, the PB-phase metasurface also acts as a half-waveplate for polarization conversion. However, the half-waveplate condition does not coincide with the antireflection condition. Moreover, materials with a high refractive index are suitable as dielectric metasurfaces; however, they usually lead to impedance mismatch at the interface. Consequently, the PB-phase metasurface suffers from severe Fresnel reflection loss.

A traditional antireflective thin-film consists of single or multiple homogeneous layers and has refractive indices and thicknesses suitable for reducing the Fresnel reflection at the interface. Sub-wavelength structures, such as gratings²², pillars^{23,24}, pyramids^{25,26}, and moth-eyes^{27–29}, may also be used for

antireflection. These structures generate a gradient effective refractive index to reduce the refractive index contrast between air and the medium through which light is entering. Nowadays, sub-wavelength structure-based antireflection has been widely used for photovoltaic solar cells³⁰.

Macroscopically, a dielectric PB-phase metasurface is an optically anisotropic medium that is similar to a birefringent structure. In 2001, Mohammed *et al.* applied an antireflection coating on smooth surfaces by exploiting the anisotropic nano-topology of a liquid-crystal polymer film³¹. In 2018, Zhu used three laminating layers as a broadband antireflection coating for a birefringent sapphire waveplate³². The aforementioned studies investigated reflection from a homogeneous and anisotropic layer. However, microscopically, as the dimension of meta-atoms is close to the incident light wavelength, the metasurface should be considered an inhomogeneous, but not a homogeneous, anisotropic medium.

In this work, we investigated the antireflection layer for the PB-phase metasurface. First, we discussed whether the traditional antireflection layer is suitable for the dielectric PB-phase metasurface. Then, an antireflection structure was proposed to enhance the efficiency of the metasurface. We then numerically investigated the overall polarization conversion efficiency (PCE) and optical properties of both gallium nitride (GaN) and niobium oxide (Nb_2O_5) nano-fins with an antireflection structure. To obtain the highest PCE, the thickness of the nano-fin was corresponded to a half-waveplate. Magnesium fluoride (MgF_2), a common low-index material for antireflection, was chosen as the antireflection layer. Here, we simulated the overall PCE enhancement and optical properties with three different arrangements of the MgF_2 layer. Based on the calculated results, an antireflection structure for the dielectric PB-phase metasurface was proposed. Thus, antireflection for the metasurface is crucial for enhancing the efficiency as well as reducing the background signal of a meta-device.

Results And Discussions

As shown in Fig. 1(a), the basic building block is a GaN nano-fin on a silica substrate. The nano-fin had its basic dimensions fixed (length: 300 nm, width: 100 nm, and period: 330 nm), while its thickness (d_f) was varied for the analysis of corresponding optical properties. All simulations were performed using the finite-difference time domain method, which is used to simulate the PCE and transmittance. In this work, incident light was assumed to be normally incident at a wavelength of 633 nm. The polarization state was x-linear polarization (XLP) propagating along the z-direction from bottom to up, as shown in Fig. 1(a). The inclined angle between the x-axis and the long axis of the nano-fin was set at 45° . Under this assumption, the PCE and transmittance were identical to a circular polarized light normally incident on a nano-fin at an arbitrary rotation angle. The XLP incident light was denoted by E_{x-in} . After passing through the nano-fin, the polarization state varied because of the anisotropy of the nano-fin. Therefore, the output component of the E -field (denoted by E_{out}) consisted of E_{x-out} and E_{y-out} which represented E_x and E_y components at the output plane, respectively. The PCE can be calculated as follows:

$$\frac{|E_{y-out}|^2}{|E_{out}|^2} \times 100\% = \frac{|E_{y-out}|^2}{|E_{x-out}|^2 + |E_{y-out}|^2} \times 100\%$$

1

For PB-phase metasurfaces, the PCE is occasionally used to evaluate the efficiency. However, emphasis is mostly on the overall efficiency, which is the ratio of the signal light intensity to the incident light intensity. Therefore, transmittance and overall PCE must be determined.

The transmittance is defined as follows:

$$\frac{|E_{out}|^2}{|E_{x-in}|^2} \times 100\% = \frac{|E_{x-out}|^2 + |E_{y-out}|^2}{|E_{x-in}|^2} \times 100\%$$

2

Finally, the overall PCE can be defined as PCE multiplied by transmittance, as given below:

$$\frac{|E_{y-out}|^2}{|E_{x-in}|^2} \times 100\%$$

3

The overall PCE is more appropriate for describing the overall efficiency of a PB-phase unit cell, which considers both transmittance and PCE. Figure 1(b) depicts the transmittance, PCE, and overall PCE as a function of the thickness (d_1) of the GaN nano-fin. The square, circle, and triangle represent the transmittance, PCE, and overall PCE, respectively. The peak of the PCE is at $d_1 = 1050$ nm, corresponding to the half-waveplate condition for polarization conversion. However, due to the yellow-band absorption of GaN, caused by Ga vacancies or their complexes^{33,34}, GaN is lossy at $\lambda = 633$ nm and the corresponding refractive index is $n + ik = 2.29 + 0.061i$. Therefore, transmittance decreased with an increase in thickness. After considering the contribution of transmittance, the highest overall PCE was believed to appear at $d_1 = 950$ nm.

Here, we considered three different cases of the MgF_2 -based antireflection structure for reducing the reflection loss of GaN nano-fins. The first was the GaN nano-fin deposited on a flat MgF_2 film over a silica substrate, which is the most intuitive antireflection structure (denoted by the green square in Figure (2)). The second (denoted by the red circle) was a GaN nano-fin stacked on a MgF_2 nano-fin, which was fabricated through standard lithography and reactive-ion etching. This is a hetero-nano-fin. For convenience, the second nano-fin is called the GaN/ MgF_2 nano-fin. Moreover, the MgF_2 nano-structure had the same geometric parameters as the nano-fin in the x and y directions. Finally, the third nano-fin (denoted by the blue triangle) was a MgF_2 nano-fin stacked on the GaN nano-fin and was called a MgF_2/GaN nano-fin. Same as the previous case, the geometric parameters of MgF_2 and GaN nano-fins were identical in the x and y directions. The simulation results of the overall PCE, PCE, and transmittance

as a function of MgF_2 thickness are displayed in Fig. 2(a), (b), and (c), respectively. For $d_1 = 1050$ nm, the flat MgF_2 film (green square) barely contributed to the PCE, overall PCE, and transmittance even with an increase in the thickness. Therefore, this case was used as a reference. For the GaN/MgF_2 nano-fin (red circle), a noticeable oscillation of overall PCE was observed with an increase in MgF_2 thickness. When MgF_2 thickness increased, the PCE curve oscillated and became lower, which was because the anisotropic OPD of nano-fin is away from the optimal optimized thickness of the half-waveplate (as mentioned in Fig. 1(b)). At the same time, the GaN/MgF_2 nano-fin positively contributed to transmittance. Although a 0.5% increase in transmittance was observed for $\text{MgF}_2 = 60$ nm, the transmittance was suppressed for most thicknesses. Notably, the overall PCE was significantly improved for the MgF_2/GaN nano-fin. The overall PCE increased from 52.7–54% when MgF_2 thickness increased from 0 to 140 nm. Although the overall PCE oscillated with varying MgF_2 thickness, the overall PCE constantly improved, compared with a bare GaN nano-fin. Because the GaN nano-fin with a thickness of 1050 nm already had the highest PCE, only a tiny increment was observed in the PCE after the addition of the MgF_2 nano-structure. Therefore, improvement in the overall PCE is believed to be mainly contributed by transmittance. Figure 2(c) shows a good agreement that transmittance improves from 54.4–55.7%. Figure 2(d), (e), and (f) depict the overall PCE, PCE, and transmittance for $d_1 = 950$ nm, which is the optimal thickness of the bare GaN nano-fin for the overall PCE. Compared with $d_1 = 1050$ nm, both GaN/MgF_2 and MgF_2/GaN nano-fins showed an improved overall PCE for $d_1 = 950$ nm, as shown in Fig. 2(d). Both PCE and transmittance exhibited significant improvement. The MgF_2 nano-structure simultaneously played a role in polarization conversion and antireflection. The increasing thickness allowed the anisotropic OPD to match the optimal half-waveplate condition. Therefore, the PCE for both GaN/MgF_2 and MgF_2/GaN nano-fins improved with an increase in MgF_2 thickness. For transmittance, behaviors of GaN/MgF_2 and MgF_2/GaN differed with increasing MgF_2 thickness. Although GaN/MgF_2 enhanced transmittance to 1.3% at a MgF_2 thickness of 260 nm, the transmittance was generally reduced for other thicknesses of MgF_2 . By contrast, the transmittance of MgF_2/GaN was constantly improved regardless of the variation in MgF_2 thickness. The flat MgF_2 layer made no contribution to overall PCE for both $d_1 = 1050$ or 950 nm. This means that the hetero-structure is necessary for antireflection.

For a homogeneous medium, the Goos–Hanchen phase is π when the incident angle is less than the total reflection angle³⁵. In our case, an optical anisotropic nano-fin was considered. The reflected phase is no more exactly equal to π owing to anisotropy, depolarization, and scattering. Here, a simple optical isolator was used for comparison. Right-circularly polarized (RCP) light normally impinges on an optical homogeneous and anisotropy film, that is, a half-waveplate. After traveling to the top of the film–air interface, part of the light reflects and back travels to the input plane. An antireflection structure allows incident and reflection beams to destructively interfere. The Jones matrix of the input and reflected light can be represented as follows:

$$E_{out} = R(-\theta) \begin{pmatrix} e^{-i\frac{\Gamma}{2}} & 0 \\ 0 & e^{i\frac{\Gamma}{2}} \end{pmatrix} R(\theta) \begin{pmatrix} 1 & 0 \\ 0 & -1 \end{pmatrix} R(-\theta) \begin{pmatrix} e^{-i\frac{\Gamma}{2}} & 0 \\ 0 & e^{i\frac{\Gamma}{2}} \end{pmatrix} R(\theta) \frac{1}{\sqrt{2}} \begin{pmatrix} 1 \\ -i \end{pmatrix}$$

4

where θ is the phase retardation and R is the rotation matrix:

$$R(-\theta) = \begin{pmatrix} \cos(\theta) & \sin(\theta) \\ -\sin(\theta) & \cos(\theta) \end{pmatrix}$$

5

As the RCP travels at the quarter-waveplate position, the polarization state converts to XLP. At the top of the film–air interface, polarization states of the incident and reflected light are left-circularly polarized (LCR) and RCP, respectively. When light back travels to the quarter-waveplate position, the polarization state converts to y-linear polarization. Finally, at the input plane, the back-reflected light is LCP, which is orthogonal to the input light. Thus, the vector product of the input and reflected light is zero. Therefore, the input and reflected light cannot interfere, and thus, a conventional thin-film antireflection coating is not suitable for reducing the Fresnel reflection loss of a homogeneous and anisotropy film.

In our nano-fin, the Goos–Hanchen reflection phase from the structure is not only equal to π but also has phase anisotropy. Therefore, polarization states of forward and backward propagation light are not completely orthogonal in our discussed PB-phase nano-fin system. We thus can realize antireflection in the PB-phase system.

Figure 3 presents the phase distribution at the upper interface of the nano-fin coated with four antireflection structures: bare nano-fin, nano-fin with a flat MgF_2 film, GaN/MgF_2 nano-fin, and MgF_2/GaN nano-fin. The corresponding phase distributions are presented in Fig. 3(a), (b), (c), and (d). Here, the thickness of GaN and MgF_2 was fixed at 950 and 140 nm, respectively. To analyze phase distribution intuitively, we calculated the standard deviation of the phase and marked it as σ . Figure 3(a) depicts that the σ of the bare nano-fin is 0.7201, which can be considered as a reference. We first observed that the σ of the nano-fin with the flat MgF_2 film was 0.7212, as shown in Fig. 3(b). Compared with the reference, the flat MgF_2 film contributed inconspicuously to the antireflection effect. The σ of the GaN/MgF_2 nano-fin was 0.7565. Compared with the flat MgF_2 film, phase distribution on the interface changed drastically, corresponding to the decreases in efficiency. As shown in Fig. 2(d), the GaN/MgF_2 nano-fin exhibited lower overall PCE at a MgF_2 thickness of 140 nm. Finally, the σ of the MgF_2/GaN nano-fin was 0.3277, as shown in Fig. 3(d). Compared with the flat MgF_2 film, the variation in phase distribution on the interface was mitigated and transmittance was increased.

As mentioned above, GaN suffers from absorption loss in the visible range. The optical characteristics of material loss make improving the overall PCE difficult. Therefore, materials without absorption loss in the

visible range must be identified. For example, Choudhury et al. comprehensively surveyed a dielectric material for a dielectric metasurface for visible and IR spectral ranges³⁶. They suggested silicon nitride (Si_3N_4) and titanium oxide (TiO_2) as good metasurfaces in visible range applications.

In addition to absorption loss, the refractive index is crucial for fabrication. Both the propagation phase and anisotropy are positively related to the refractive index. Therefore, a high aspect ratio is required to accumulate sufficient phase modulation for materials with a relatively low refractive index. We thus focused on dielectric materials that can be applied in the visible range and have a high refractive index. Figure 4 depicts the optimized thickness (d_2) of nano-fins based on various materials. As shown in the inset of Fig. 4, geometric parameters were all fixed (length, 300 nm; width, 100 nm; and period, 330 nm). Recently, Prof. Tsai's group demonstrated a GaN structure with an aspect ratio as high as 10–20 for high efficiency^{18,37,38}. However, fabricating a nano-fin with such a high aspect ratio is extremely challenging. Thus, we used the geometric parameters of the GaN nano-fin as a benchmark for the state-of-the-art fabrication. Nano-fins with an optimized thickness higher than that of GaN nano-fin were excluded as candidates for a high-efficiency dielectric metasurface. According to this criterion, Si_3N_4 , tantalum pentoxide (Ta_2O_5), and sputtering TiO_2 are not suitable materials. Compared with GaN, both anatase and rutile TiO_2 have the advantages of higher efficiency and lower aspect ratio. However, the crystalline phase control of TiO_2 during deposition is severe. Thus, crystalline TiO_2 is also excluded. Amorphous silicon (a-Si) is a material with a high refractive index and can be easily processed using standard semiconductor-compatible manufacturing techniques. However, it suffers from huge absorption loss in the visible range, which makes it inappropriate. Finally, Nb_2O_5 offers a fair refractive index and low absorption ($n + ik = 2.32 + 0i$), making it suitable for visible applications. Therefore, we believe that Nb_2O_5 is suitable for high-efficient dielectric metasurfaces.

We simulated the optical response of a nano-fin composed of Nb_2O_5 patterned on the same substrate at an incident wavelength of 633 nm, as shown in Fig. 5(a). The polarization state was XLP propagating along the z-direction. Figure 5(b) depicts the transmittance, PCE, and overall PCE as a function of the thickness (d_3) of the Nb_2O_5 nano-fin. Corresponding to the half-waveplate condition for polarization conversion, the peak of the PCE appeared at $d_3 = 1000$ nm. Because Nb_2O_5 does not suffer absorption loss in the visible range, which can be easily observed, transmittance did not decrease with an increase in d_3 . Therefore, same as the PCE, the highest overall PCE appeared at $d_3 = 1000$ nm. As expected, the overall PCE of Nb_2O_5 was considerably higher than that of the GaN nano-fin. By contrast, an obvious dip appeared at $d_3 = 1100$ nm, which is caused by guided-mode resonance³⁹.

We also considered three different cases of the MgF_2 -based antireflection layer for reducing the reflection loss of the Nb_2O_5 nano-fin: a flat MgF_2 film under the nano-fin, $\text{Nb}_2\text{O}_5/\text{MgF}_2$ nano-fin, and $\text{MgF}_2/\text{Nb}_2\text{O}_5$ nano-fin, which are denoted by a green square, red circle, and blue triangle, respectively, in Fig. 6. Here, the thickness (d_3) of Nb_2O_5 for all cases was 1000 nm. The simulation results of the overall PCE, PCE, and transmittance as a function of MgF_2 thickness are presented in Fig. 6(a), (b), and (c), respectively. First, a

flat MgF_2 film in the Nb_2O_5 system barely contributed to the PCE, overall PCE, and transmittance. Therefore, this case was marked as a reference. Both $\text{Nb}_2\text{O}_5/\text{MgF}_2$ and $\text{MgF}_2/\text{Nb}_2\text{O}_5$ nano-fins exhibited obvious enhancement of the overall PCE (Fig. 6(a)). The highest overall PCE of both $\text{Nb}_2\text{O}_5/\text{MgF}_2$ and $\text{MgF}_2/\text{Nb}_2\text{O}_5$ nano-fins was 94.6% when MgF_2 thickness was 160 and 140 nm, respectively. The thickness of the Nb_2O_5 nano-fin ($d_3 = 1000$ nm) was already an optimal optimized half-waveplate. For both $\text{Nb}_2\text{O}_5/\text{MgF}_2$ and $\text{MgF}_2/\text{Nb}_2\text{O}_5$ nano-fins, an additional MgF_2 layer forced the nano-fin away from the optimal optimized thickness of the half-waveplate and decreased the PCE (Fig. 6(b)). Thus, transmittance enhancement contributed to all the improvement in the overall PCE. Figure 6(c) shows a transmittance of 94.7% for both $\text{Nb}_2\text{O}_5/\text{MgF}_2$ and $\text{MgF}_2/\text{Nb}_2\text{O}_5$ nano-fins. Although both these nano-fins exhibited a good enhancement of the overall PCE, the $\text{MgF}_2/\text{Nb}_2\text{O}_5$ nano-fin attained thickness efficiency at a lower MgF_2 thickness. Thus, the antireflection layer located on the top of a nano-fin is considered more suitable.

As mentioned above, MgF_2 contributed negatively to the PCE and reduced the overall PCE when the nano-fin thickness was under an ideal half-waveplate condition. Therefore, we further optimized the hetero-nano-fin to ensure that the Nb_2O_5 nano-fin was slightly thinner than the ideal half-waveplate condition. Figure 7 presents the overall PCE as a function of MgF_2 and Nb_2O_5 thicknesses. The color represents the overall PCE. Warm and cold colors represent the enhanced and suppressed overall PCE, respectively, compared with the bare Nb_2O_5 nano-fin. In this calculation, MgF_2 was located on the top of the Nb_2O_5 nano-fin. As the thickness of Nb_2O_5 was 950 nm, the overall PCE improved from 91–96% when MgF_2 thickness increased from 0 to 140 nm. At this time, MgF_2 made up for a shortage in the ideal half-waveplate condition. MgF_2 plays a role in both polarization conversion and antireflection. Moreover, the overall PCE of the $\text{MgF}_2/\text{Nb}_2\text{O}_5$ nano-fin was 1.7 times higher than that of the MgF_2/GaN nano-fin. Therefore, we believe that the $\text{MgF}_2/\text{Nb}_2\text{O}_5$ hetero-nano-fin is a highly efficient candidate for dielectric metasurfaces.

Conclusions

In summary, we numerically investigated the enhancement of overall PCE of hetero-nano-fins by using GaN and Nb_2O_5 nano-fins with three types of antireflection structure: an intuitive flat MgF_2 layer under nano-fins, nano-fins/ MgF_2 , and MgF_2 /nano-fins. Compared with the flat antireflection layer, a hetero-nano-fin exhibited a better overall PCE enhancement. Both GaN/ MgF_2 and MgF_2 /GaN nano-fins improved PCE with an increase in MgF_2 thickness. Compared with the GaN/ MgF_2 nano-fin, the MgF_2 /GaN nano-fin led to higher overall PCE enhancement. For the MgF_2 /GaN nano-fin, the overall PCE improved from 52.7–54% with an increase in MgF_2 thickness from 0 to 140 nm. Unfortunately, the absorption loss of GaN in the visible range limited its overall PCE. By contrast, lossless Nb_2O_5 was considered because of its high refractive index. The overall PCE of the Nb_2O_5 -based nano-fin was 1.7 times higher than that of the GaN-based nano-fin. Moreover, an overall PCE up to 96% was achieved after optimization. Antireflection

coating for a metasurface is crucial for enhancing the efficiency and reducing the background signal of a meta-device.

Methods

All simulation results were performed with the FDTD methods. All nano-fins were simulated with periodic boundary conditions in xz and yz-planes; absorbing boundary in xy-planes. The incident wavelength was 633 nm with x-polarized. The refractive index of silica substrate, GaN, and Nb₂O₅ are $1.45 + 0i$, $2.29 + 0.061i$, and $2.32 + 0i$ at 633 nm, respectively.

Declarations

Acknowledgments

The authors acknowledge financial support from Ministry of Science and Technology, Taiwan (Grant Nos. MOST 110-2124-M-008-002 and 110-2221-E-008-060-MY3). This manuscript was edited by Wallace Academic Editing.

Author contributions

Y.-H. L. and W.-L. H. designed and performed the simulations and data analysis; W.-L. H. wrote the manuscript; C.-M. W developed the theoretical aspect, analyzed the result, and prepared the manuscript. All authors commented on the manuscript.

Conflicts of interests

The author(s) declare no competing interests.

Data availability

All data generated or analysed during this study are included in this published article (and its Supplementary Information files)

References

1. Sun S., *et al.* High-efficiency broadband anomalous reflection by gradient meta-surfaces. *Nano Lett.* **12**, 6223-6229 (2012).
2. Hsu W. L., *et al.* Vertical split-ring resonator based anomalous beam steering with high extinction ratio. *Sci. Rep.* **5**, 11226 (2015).
3. Chen W. T., *et al.* High-efficiency broadband meta-hologram with polarization-controlled dual images. *Nano Lett.* **14**, 225-230 (2014).

4. Lu D., & Liu Z. Hyperlenses and metalenses for far-field super-resolution imaging. *Nat. Commun.* **3**, 1205 (2012).
5. Yu N., *et al.* Light propagation with phase discontinuities: generalized laws of reflection and refraction. *Science* **334**, 333-337 (2011).
6. Konishi K., Kan T., & Kuwata-Gonokami M. Tunable and nonlinear metamaterials for controlling circular polarization. *J. Appl. Phys.* **127**, 23 (2020).
7. Epstein A., & Eleftheriades G. V. Huygens' metasurfaces via the equivalence principle: design and applications. *J. Opt. Soc. Am. B* **33** A31-A50 (2016).
8. Decker M., *et al.* High-Efficiency Dielectric Huygens' Surfaces. *Adv. Opt. Mater.* **3**, 813-820 (2015).
9. Kerker M., Wang D. S., & Giles C. L. Electromagnetic scattering by magnetic spheres. *J. Opt. Soc. Am.* **73**, 765–767 (1983).
10. Arbabi A., Horie Y., Ball A. J., Bagheri M., & Faraon A. Subwavelength-thick lenses with high numerical apertures and large efficiency based on high-contrast transmitarrays. *Nat. Commun.* **6**, 7069 (2015).
11. She A., Zhang S., Shian S., Clarke D. R., & Capasso F. Adaptive metalenses with simultaneous electrical control of focal length, astigmatism, and shift. *Sci. Adv.* **4**, eaap9957 (2018).
12. Emani N. K., *et al.* High-efficiency and low-loss gallium nitride dielectric metasurfaces for nanophotonics at visible wavelengths. *Appl. Phys. Lett.* **111**, 22 (2017).
13. Koirala I., Lee S. S., & Choi D. Y. Highly transmissive subtractive color filters based on an all-dielectric metasurface incorporating TiO₂ nanopillars. *Opt. Express* **26**, 18320-18330 (2018).
14. Jang M., *et al.* Wavefront shaping with disorder-engineered metasurfaces," *Nat. Photonics* **12**, 84-90 (2018).
15. Khorasaninejad M., Chen W. T., Devlin R. C., Oh J., Zhu A. Y., & Capasso F. Metalenses at visible wavelengths: Diffraction-limited focusing and subwavelength resolution imagin. *Science* **352**, 1190–1194 (2016).
16. Song Q., *et al.* Ptychography retrieval of fully polarized holograms from geometric-phase metasurfaces. *Nat. Commun.* **11**, 2651 (2020).
17. Qin F. F., Liu Z. Z., Zhang Z., Zhang Q., & Xiao J. J. Broadband full-color multichannel hologram with geometric metasurface. *Opt. Express* **26**, 11577-11586 (2018).
18. Chen B. H., *et al.* GaN Metalens for Pixel-Level Full-Color Routing at Visible Light. *Nano. Lett.* **17**, 6345-6352 (2017).
19. Lee G. Y., *et al.* Metasurface eyepiece for augmented reality. *Nat. Commun.* **9**, 4562 (2018).
20. Chen W. T., Zhu A. Y., Sisler J., Bharwani Z., & Capasso F. A broadband achromatic polarization-insensitive metalens consisting of anisotropic nanostructures. *Nat. Commun.* **10**, 355 (2019).
21. Xu H. X., Wang G. M., Cai T., Xiao J., & Zhuang Y. Q. Tunable Pancharatnam-Berry metasurface for dynamical and high-efficiency anomalous reflection. *Opt. Express* **24**, 27836-27848 (2016).
22. Tsai T. Y., Lee Z. C., Tsao H. X., & Lin S. T. Minimization of Fresnel reflection by anti-reflection fiber Bragg grating inscribed at the fiber ends. *Opt. Express* **27**, 11510-11515 (2019).

23. Motamedi M. E., Southwell W. H., & Gunning W. J. Antireflection Surfaces in Silicon Using Binary Optics Technology. *Appl. Opt.* **31**, 4371-4376 (1992).
24. Proust J., Fehrembach A. L., Bedu F., Ozerov I., & Bonod N. Optimized 2D array of thin silicon pillars for efficient antireflective coatings in the visible spectrum *Sci. Rep.* **6**, 24947 (2016).
25. Ge S. B., *et al.* Design and Preparation of a Micro-Pyramid Structured Thin Film for Broadband Infrared Antireflection. *Coatings* **8** (2018).
26. Yue Z. H., Shen H. L., & Jiang Y. Antireflective nanostructures fabricated by reactive ion etching method on pyramid-structured silicon surface. *Appl. Surf. Sci.* **271**, 402-406 (2013).
27. Brunner R., *et al.* Antireflective "moth-eye" structures on tunable optical silicone membranes. *Appl. Opt.* **51**, 4370-4376 (2012).
28. Song Y. M., Jeong Y., Yeo, C. I. & Lee Y. T. Enhanced power generation in concentrated photovoltaics using broadband antireflective coverglasses with moth eye structures. *Opt. Express* **20**, A916-923 (2012).
29. Weiblen R. J., *et al.* Irradiance enhancement and increased laser damage threshold in As(2)S(3) moth-eye antireflective structures. *Opt. Lett.* **40**, 4799-4802 (2015).
30. Peng Y. J., Huang H. X., & Xie H. Rapid fabrication of antireflective pyramid structure on polystyrene film used as protective layer of solar cell. *Sol. Energy Mater. Sol. Cells* **171**, 98-105 (2017).
31. Ibn-Elhaj M. & Schadt M. Optical polymer thin films with isotropic and anisotropic nano-corrugated surface topologies. *Nature* **410**, 796-799 (2001).
32. Zhu C. Broadband antireflection coatings adopting 3-layer homogeneous dielectric materials for birefringent sapphire waveplate in millimeter-wave band. *Aip. Adv.* **8** (2018).
33. Neugebauer J. & Van de Walle C. G. Gallium vacancies and the yellow luminescence in GaN. *Appl. Phys. Lett.* **69**, 503-505 (1996).
34. Saarine K. *et al.* Observation of native Ga vacancies in GaN by positron annihilation. *Phys. Rev. Lett.* **79**, 3030-3033 (1997).
35. Renard R. H. Total Reflection: A New Evaluation of the Goos–Hänchen Shift. *J. Opt. Soc. Am.* **54**, 1190-1197 (1964).
36. Choudhury S. M., *et al.* Material platforms for optical metasurfaces. *Nanophotonics* **7**, 959-987 (2018).
37. Lin R. J., *et al.* Achromatic metalens array for full-colour light-field imaging. *Nat. Nanotechnol* **14**, 227-231 (2019).
38. Li L., *et al.* Metalens-array-based high-dimensional and multiphoton quantum source. *Science* **368**, 1487-1490 (2020).
39. Chen Y.-C., Zeng Q.-C., Yu C.-Y., & Wang C.-M. General case of the overall phase modulation through a dielectric PB-phase metasurface. *OSA Continuum.* **4**, 3204-3212 (2021).

Figures

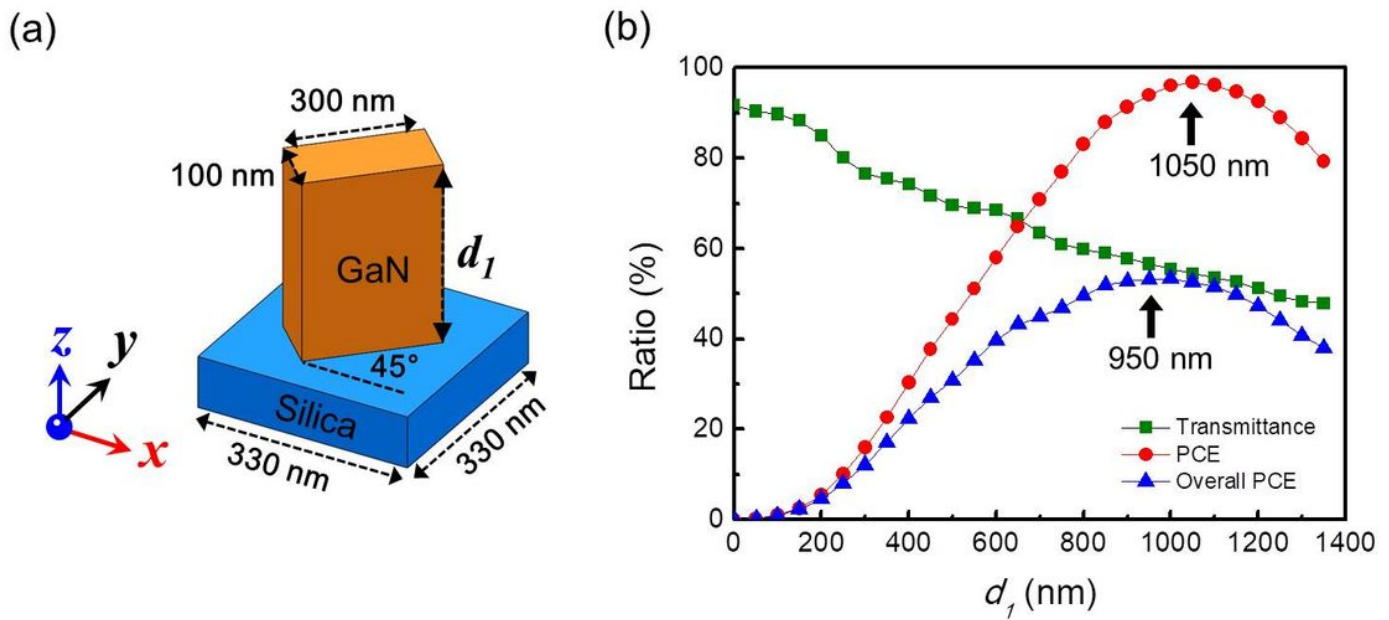


Figure 1

Geometric diagram and optical property of GaN nano-fin. (a) Geometric diagram of a GaN nano-fin on a silica substrate, where d_1 is the thickness of the nano-fin. (b) Transmittance, PCE, and overall PCE versus the thickness of the nano-fin under light illumination of 633 nm at normal incidence along the z-direction from bottom to up. The polarized light is along the x-direction. The light is x-polarized, with $\lambda = 633$ nm. The light impinges perpendicularly onto the structure from bottom along the positive z-direction.

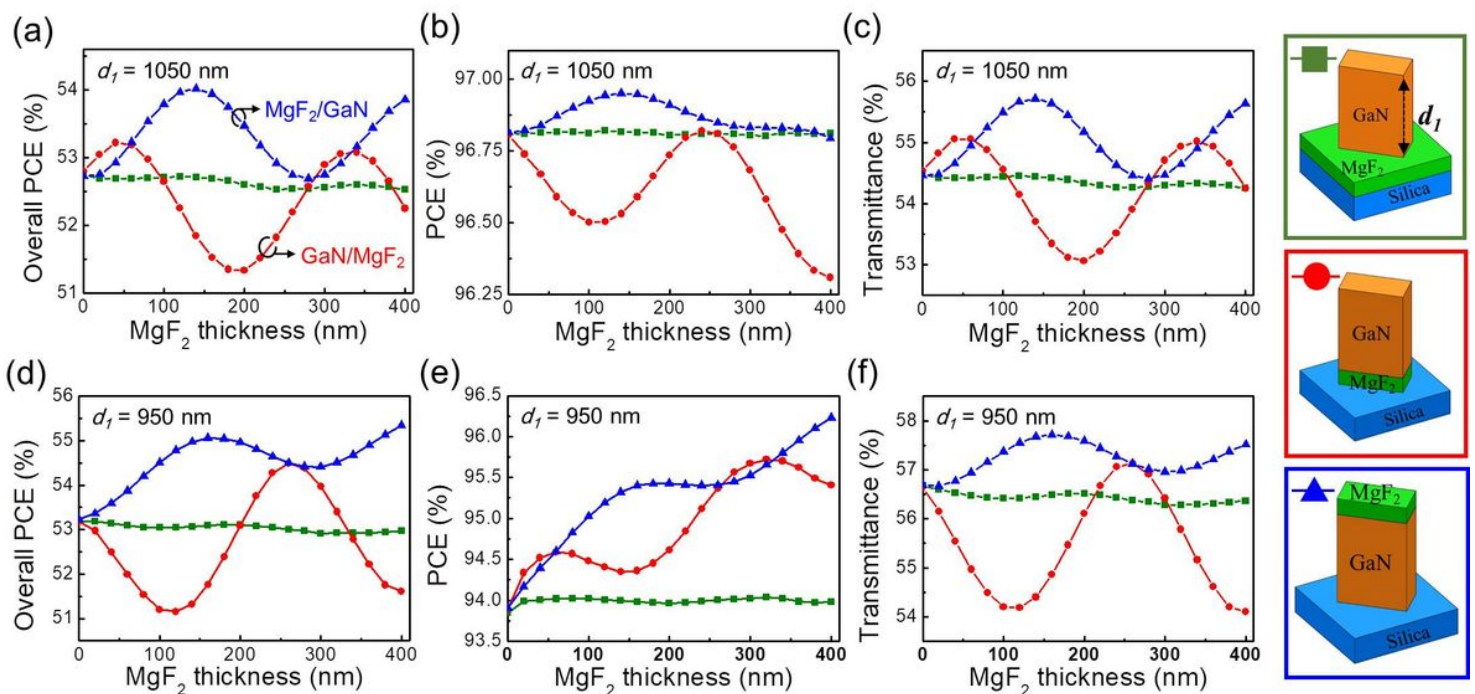


Figure 2

Optical property of GaN nano-fin consisted with MgF₂ layer. Simulation results of (a) overall PCE, (b) PCE, and (c) transmittance versus MgF₂ thickness with $d_1 = 1050$ nm. Simulation results of (d) overall PCE, (e) PCE, and (f) transmittance versus MgF₂ thickness with $d_1 = 950$ nm. The green square denotes a flat MgF₂ film deposited under a GaN nano-fin, the red circle denotes a GaN nano-fin located on the top of the MgF₂ nano-structure, and the blue triangle denotes a MgF₂ nano-structure stacked on the top of a GaN nano-fin.

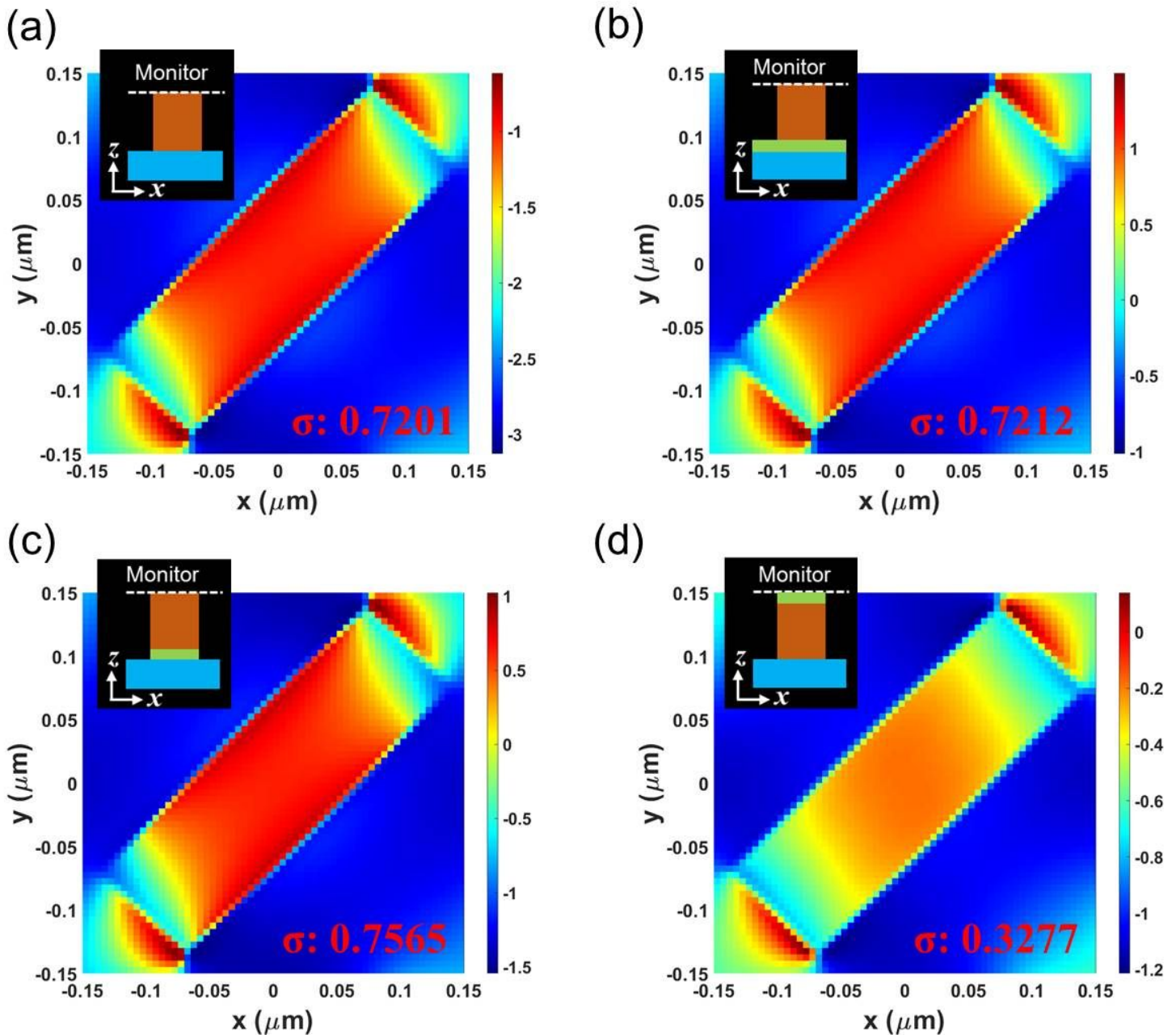


Figure 3

Electric field distribution of nano-fin structures. Simulations of phase distribution at the upper interface of the nano-fin for the (a) nano-fin without MgF₂, (b) flat MgF₂ film, (c) nano-fin stacking on the MgF₂ nano-

structure, and (d) MgF_2 nano-structure stacking on a nano-fin. σ is the standard deviation of phase distribution at the upper interface.

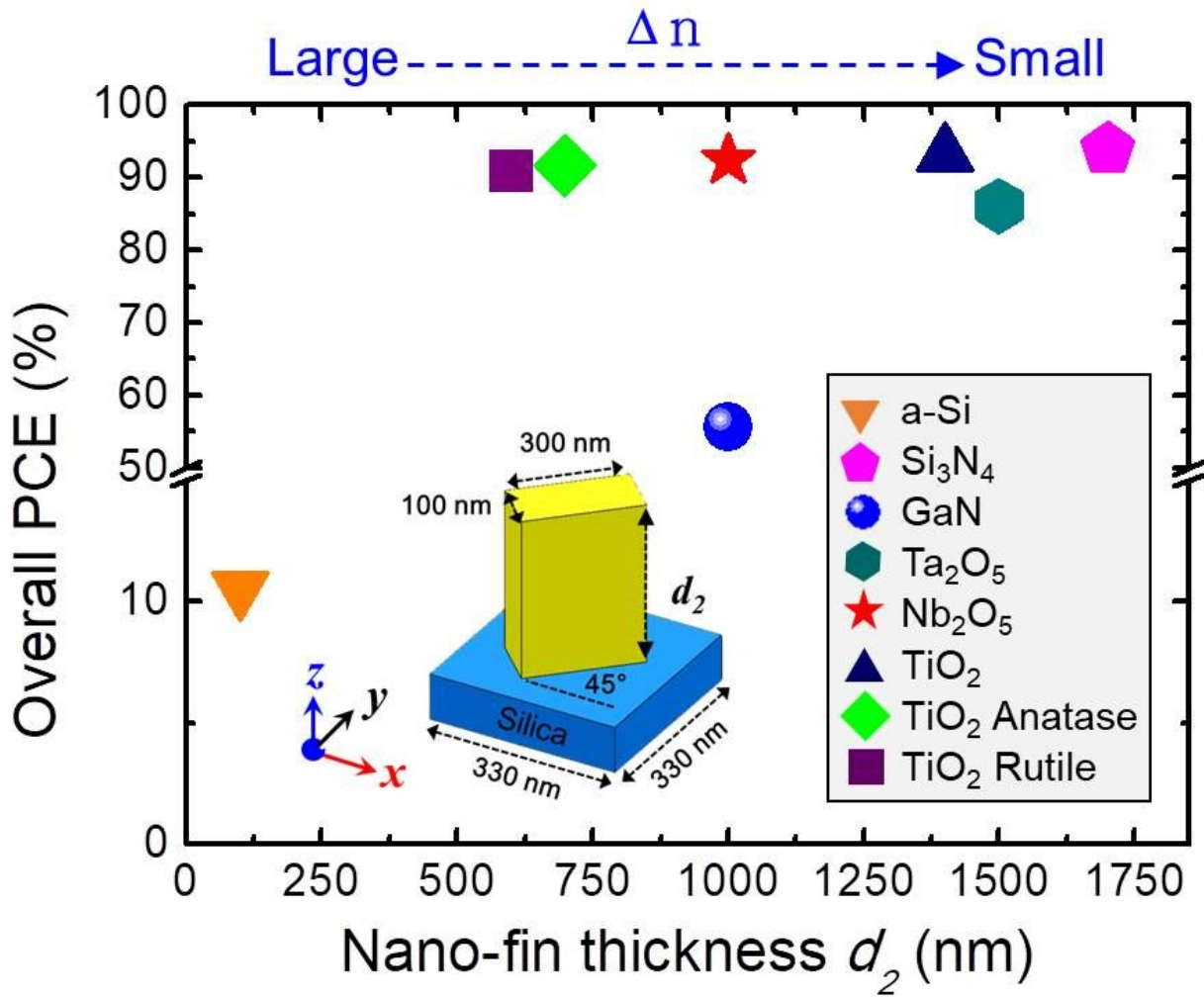


Figure 4

Overall PCE comparison. Optimized thickness (d_2) of a nano-fin for various materials at the highest overall PCE. The geometric diagram of a meta-atom is shown in inset.

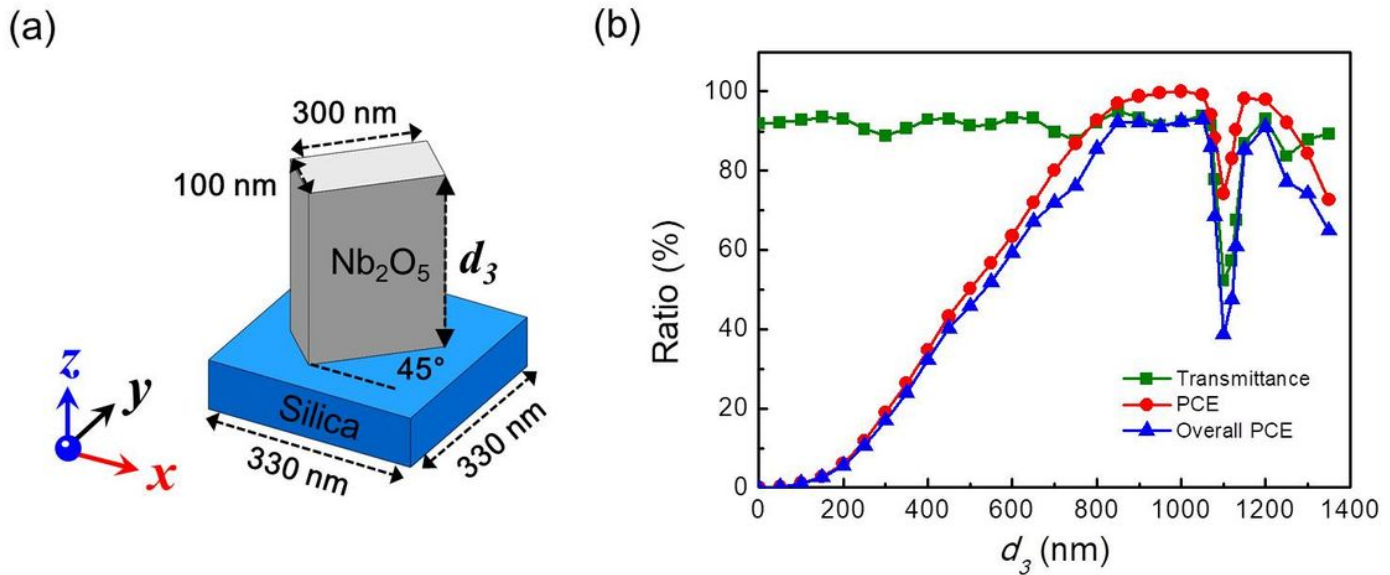


Figure 5

Geometric diagram and optical property of Nb_2O_5 nano-fin. (a) Schematic of a Nb_2O_5 nano-fin on a silica substrate, where d_3 is the thickness of the Nb_2O_5 nano-fin. (b) Transmittance, PCE, and overall PCE versus the thickness of the Nb_2O_5 nano-fin. x-polarized light with $\lambda = 633$ nm impinges perpendicularly onto the structure from bottom along the positive z-direction.

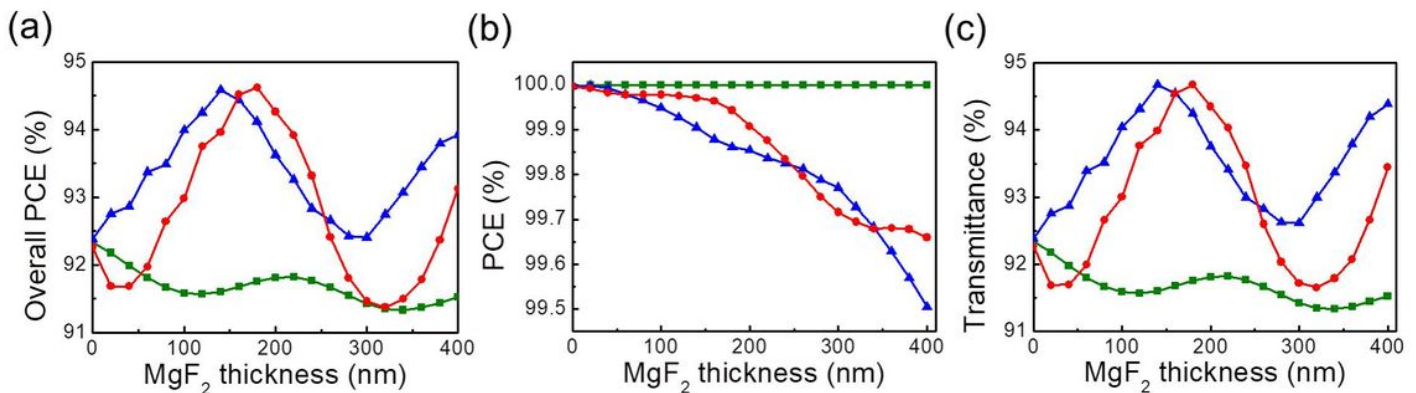


Figure 6

Optical property of Nb_2O_5 nano-fin consisted with MgF_2 . Simulation results of (a) overall PCE, (b) PCE, and (c) transmittance as a function of MgF_2 thickness. The thickness of Nb_2O_5 is fixed to be $d_3 = 1000$ nm. The green square denotes a flat MgF_2 film deposited under the Nb_2O_5 nano-fin, the red circle denotes a nano-fin located on the top of the MgF_2 nano-structure, and the blue triangle denotes a MgF_2 nano-structure stacked on the top of a nano-fin.

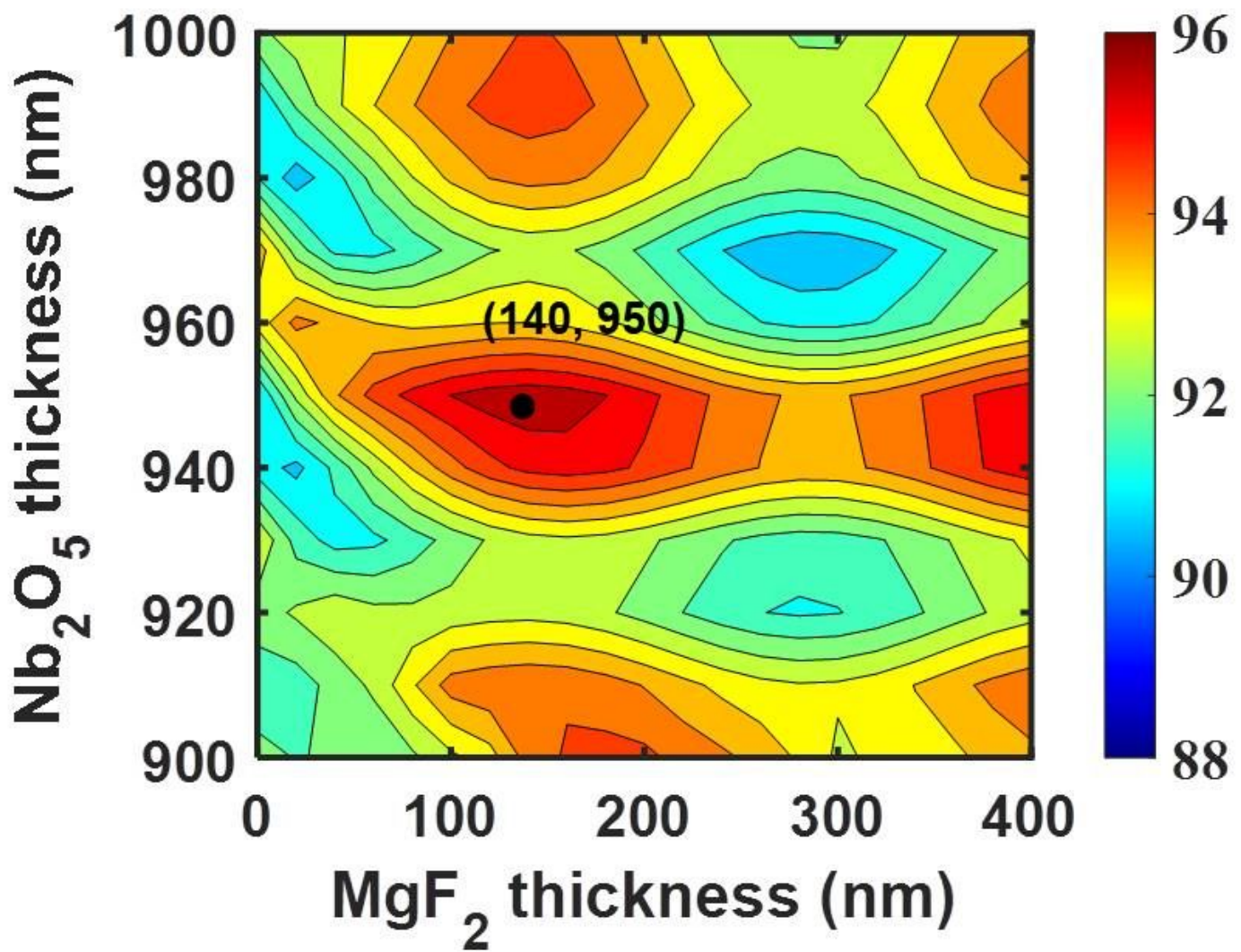


Figure 7

Overall PCE mapping of MgF₂/Nb₂O₅ hetero-nano-fin. Simulation of overall PCE as a function of MgF₂ and Nb₂O₅ thicknesses. MgF₂ is located on the top of the Nb₂O₅ nano-fin. The black dot represents the thickness with the highest overall PCE.